



Defect topology and annihilation by cooperative movement of atoms in neutron-irradiated graphite

Ranjan Mittal ^{1,2}, Mayanak K. Gupta ¹, Sanjay K. Mishra,¹ Sourabh Wajhal,¹ Himanshu K. Poswal,³ Baltej Singh,^{1,2} Anil Bhimrao Shinde,¹ Poluri Siva Rama Krishna,¹ Peram Delli Babu,⁴ Ratikant Mishra,^{2,5} Pulya Umamaheswara Sastry,^{1,2} Rakesh Ranjan,⁶ and Samrath Lal Chaplot^{1,2}

¹*Solid State Physics Division, Bhabha Atomic Research Centre, Mumbai 400085, India*

²*Homi Bhabha National Institute, Anushaktinagar, Mumbai 400094, India*

³*High Pressure & Synchrotron Radiation Physics Division, Bhabha Atomic Research Centre, Trombay, Mumbai 400085, India*

⁴*UGC-DAE Consortium for Scientific Research, Mumbai Centre, R5-Shed, BARC, Trombay, Mumbai 400085, India*

⁵*Chemistry Division, Bhabha Atomic Research Centre, Mumbai 400085, India*

⁶*Reactor Operations Division, Bhabha Atomic Research Centre, Mumbai 400085, India*



(Received 17 April 2020; revised 29 June 2020; accepted 21 July 2020; published 6 August 2020)

Graphite has been used as a neutron moderator or reflector in many nuclear reactors. The irradiation of graphite in a nuclear reactor results in a complex population of defects. Heating of the irradiated graphite at high temperatures results in annihilation of the defects with release of an unusually large energy, called the Wigner energy. From various experiments on highly irradiated graphite samples from the CIRUS reactor at Trombay and *ab initio* simulations, we have identified various 2-, 3-, and 4-coordinated topological structures in defected graphite, and provided a microscopic mechanism of defect annihilation on heating and release of the Wigner energy. The annihilation process involves cascading cooperative movement of atoms in multiple steps involving an intermediate structure. Our work provides insights in understanding of the defect topologies and annihilation in graphite which is of considerable importance to wider areas of graphitic materials including graphene and carbon nanotubes.

DOI: [10.1103/PhysRevB.102.064103](https://doi.org/10.1103/PhysRevB.102.064103)

I. INTRODUCTION

Graphite has been used in a high-radiation environment, as a neutron moderator or reflector, in many nuclear reactors, especially research and material testing reactors such as X-10 at Oak Ridge National Laboratory (USA), the Windscale Piles (UK), and G1 (Marcoule, France). About 250 kilotons of irradiated graphite inventory is present all over the world [1]. There is much interest in understanding the change in behavior of graphite, as well as in other graphitic materials such as graphene and carbon nanotubes due to irradiation [2–10]. The hexagonal structure of graphite [11] has layers of carbon atoms formed by strong covalent bonding in the *a-b* plane. These layers are stacked along the hexagonal axis and are held by van der Waals forces. The irradiation of graphite in a nuclear reactor results in the knocking out of carbon atoms from their equilibrium sites. Defects in graphite are unusual since they involve very large potential energy and are prevented from annealing at ambient or moderately high temperatures due to a large energy barrier. Consequently, on heating of the irradiated graphite at high temperatures of around 200 °C, the annealing of the defects is spontaneous with release of an unusually large energy, called the Wigner energy [12].

Extensive studies have been reported on unirradiated graphite, graphene, and carbon nanotubes, including their highly anisotropic elastic [13,14] and thermal-expansion behavior [15–18] and spectroscopic studies [19–21] of the phonon spectrum. Experimental measurements of the phonon density of states in neutron-irradiated graphite have been very recently reported [22] along with *ab initio* calculations in a

variety of defect structures. The macroscopic measurements on irradiated graphite reveal change in the thermal and elastic properties due to damage in the structure [4,12,23–28]. Neutron irradiation damage of graphite has been studied [29] by high-resolution transmission electron microscopy and Raman spectroscopy. Earlier work on characterization of radiation damage in graphite was largely based on microscopy techniques [transmission electron microscopy (TEM), scanning tunneling microscopy (STM), etc.] and has been nicely reviewed [30]. The process of radiation damage in graphite has been simulated [31] by classical molecular dynamics simulations and *ab initio* calculations. First-principles theoretical studies of the structure, energies, and behavior of defects in graphitic materials have also been reported [3,32–35]. Reports of experimental investigation of the structure of the defects at the atomic level, such as using neutron diffraction, and *ab initio* simulations of the dynamical behavior of the knocked-out atoms, defect annealing mechanisms, and the consequent Wigner energy release are not available. Here we address these aspects using a variety of experimental techniques and first-principles dynamical simulations.

Several graphite samples [36] irradiated with neutrons at various levels of fluence were taken out from a block of irradiated nuclear-grade graphite originally used in the reflector section of the CIRUS research reactor at Trombay, India. The samples were located at various radial distances away from the reactor core. Table I includes the radial distances of various graphite samples with respect to the sample S0 which had seen the largest neutron fluence. The neutron flux at various sample locations has been estimated [36] using deterministic meth-

TABLE I. Neutron fluence as seen by various graphite samples [36]. The irradiated samples are numbered S0–S11 in the order of decreasing neutron fluence seen by them; i.e., S0 and S11 have seen the maximum and minimum neutron fluence, respectively. Another unirradiated sample for reference is assigned as sample number S12. The fluence of neutrons of energy more than 50 keV is converted to displacement per atom (dpa) by multiplying [37] by a factor of 0.68×10^{-21} dpa cm²/neutrons. The displacement per atom (dpa) is given in units of 10^{-3} . The samples are located at various radial distances away from the reactor core. The radial distances of various graphite samples are with respect to the sample S0 which had seen the largest neutron fluence.

Sample No.	Radial distance (cm)	Thermal neutrons ($\times 10^{20}$ neutrons/cm ²) ($E < 0.625$ eV)	Epithermal neutrons ($\times 10^{19}$ neutrons/cm ²) (0.625 eV $< E < 0.82$ MeV)	Fast neutrons ($\times 10^{18}$ neutrons/cm ²) ($E > 0.82$ MeV)	Displacement per atom (dpa) ($\times 10^{-3}$)
S0	0	22.06	37.69	19.99	64.5
S1	5	20.37	25.12	13.17	42.9
S2	10	18.53	16.46	8.50	28.0
S3	15	16.62	10.49	5.29	17.7
S4	20	15.09	7.38	3.70	12.5
S5	30	12.94	4.30	2.03	7.2
S6	40	10.11	1.72	0.084	2.4
S7	50	7.58	0.67	0.034	0.9
S8	60	5.38	0.29	0.016	0.4
S9	70	3.44	0.08	0.0063	0.1
S10	80	1.71	0.05	0.0033	0.07
S11	90	0.75	0.03	0.0013	0.04

ods. The neutron fluence is found to decrease with the distance away from the reactor in the reflector section. The highest fluence of the neutrons encountered by the samples is 2.6×10^{21} neutrons/cm² over a period of several decades. The neutron fluence seen by various samples is depicted in Table I. We have also used an unirradiated sample (S12) for reference. We have calculated the values of displacement per atom (dpa) for neutron energy more than 50 keV by multiplying with a factor of 0.68×10^{-21} dpa cm²/neutrons to the neutrons fluence, following Ref. [37]. Out of the total epithermal flux in the energy range of 0.625 eV–0.82 MeV, we have estimated the epithermal neutron flux for energies more than 50 keV assuming the well-known $1/E$ spectrum. The displacement per atom (dpa) for various samples is given in Table I.

The samples have been characterized by neutron and x-ray diffraction, differential scanning calorimetry, Raman scattering, and specific heat measurements and small angle x-ray scattering (Fig. S1 in the Supplemental Material [38]). The results also show that the graphite samples which have been irradiated with very high neutron fluence of epithermal and fast neutrons (exceeding 10^{19} neutrons/cm²) are significantly damaged, while the thermal neutron fluence is not so well correlated. To understand the experimental data on the structure and dynamics, we have performed *ab initio* lattice dynamics and molecular dynamics simulations to model the defects, and to identify the mechanisms of annealing of defects in neutron-irradiated graphite. While irradiation results in defects at various length scales including dislocations and clusters, our studies have focused on atomic level defects that are most relevant to the large Wigner energy release.

II. EXPERIMENTAL DETAILS

A. X-ray and neutron diffraction

X-ray diffraction studies at ambient temperature are carried out using an 18 kW rotating Cu-anode based powder diffrac-

tometer operating in the Bragg-Brentano focusing geometry with a curved crystal monochromator. Data were collected in the continuous scan mode in step intervals of 0.02° in the 2θ range of 10° – 120° . The neutron powder diffraction data on graphite samples have been recorded in the 2θ range of 4° – 138° in intervals of 0.1° on the powder diffractometer at the Dhruva Reactor in the Bhabha Atomic Research Centre, Trombay, India. The wavelength of the neutrons is 1.2443 Å. The x-ray and neutron diffraction data are analyzed using the Rietveld [39] refinement program FULLPROF [40].

B. High- Q neutron powder diffraction

The neutron powder diffraction data on graphite samples have been recorded in the Q range of up to 15 \AA^{-1} on the High- Q powder diffractometer [41] at the Dhruva Reactor in the Bhabha Atomic Research Centre, Trombay, India. The wavelength of the neutrons is 0.783 Å. The data have been analyzed by the Monte Carlo $G(r)$ method [42] to obtain the pair-distribution function.

C. Raman measurements

The Raman spectra on graphite samples were recorded using a micro Raman spectrograph Jobinyvoun T6400 with a $20\times$ objective equipped with a Peltier cooled CCD detector. The argon ion laser wavelength of 514.5 nm was used for measurements. The Lorentzian function was fitted to Raman profiles of various samples in the range from 1200 to 1800 cm^{-1} to obtain the full width at half maximum (FWHM), peak intensities, and peak positions of the D, G, and D_o modes.

D. Specific heat

Heat capacity was measured using the heat capacity option of the Quantum Design company's physical property

measurement system (PPMS), which employs the relaxation calorimetry technique.

E. Differential scanning calorimetry

Quantitative information on the extent of defects in the crystal lattice of graphite formed during irradiation of samples was determined by heating the irradiated samples in a Mettler Toledo differential scanning calorimeter (DSC-I). The DSC was calibrated for temperature and heat flow by melting high-purity In and Zn standards. About 10–15 mg of the irradiated graphite samples in the form of powder was sealed in a 40- μ l aluminum DSC pan. The samples were then heated at a rate of 5 $^{\circ}$ C/min from 25 $^{\circ}$ C to 400 $^{\circ}$ C under the flow of argon. The enthalpy changes for the process and the annihilation temperature were determined using STARE software provided by MS Mettler.

III. COMPUTATIONAL DETAILS

The first-principles density functional theory (DFT) calculations were performed using the Vienna based *ab initio* simulation package [43,44] (VASP). The generalized gradient approximation with the Perdew, Burke, and Ernzerhof [45,46] (PBE) functional implemented in VASP has been used for exchange correlation energy. The projector augmented wave method was used to incorporate the interaction between valance and core electrons. The plane wave basis set with maximum kinetic energy cutoff of 1000 eV was used. The Brillouin zone integration was performed on $20 \times 20 \times 2$ mesh generated using the Monkhorst-Pack method [47]. The convergence criteria for total energy and forces were set 10^{-8} eV and 10^{-3} eV/ \AA , respectively. The relaxation of the graphite structure was performed with including various van der Waals (vdW)-DF nonlocal correlation functionals [48–50]. We find that the relaxation performed using the optB88-vdW [50] (BO) functional scheme of the vdW-DFT method produces the best match with the experimental structure.

The structure relaxation and phonon calculations have been performed on three different configurations, one with the perfect graphite structure (space group $P6_3/mmc$) while other two configurations are with a single Frenkel defect in a 64-atom supercell ($4 \times 4 \times 1$) and a 128-atom supercell ($4 \times 4 \times 2$), respectively, with periodic boundary conditions. The Frenkel defect in the graphite structure was created by removing one carbon atom from one layer and placing it at a position away from the vacant site between the graphite layers. The defect structure was relaxed, which formed a metastable state with the interstitial carbon atom trapped between the layers. The relaxed structures in all three configurations have been used to calculate the phonon density of states. The PHONON5.2 [51] software has been used to generate the supercell and displaced configuration for phonon calculations. The partial density of states of an individual atom has been calculated by projecting the individual atomic eigenvectors on the total eigenvector.

Ab initio molecular dynamics (MD) simulation on the perfect and defected graphite structures has been performed on three configurations, namely, the perfect structure, and the

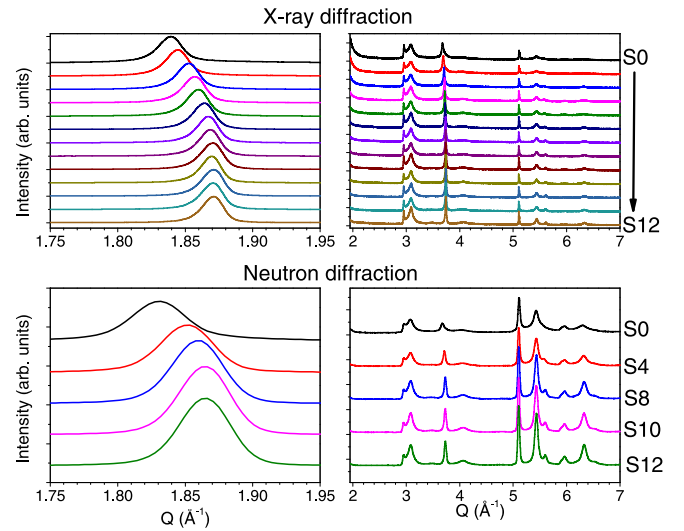


FIG. 1. Evolution of the powder x-ray and neutron diffraction pattern of unirradiated and irradiated graphite. The irradiated samples are numbered S0–S11 in the order of decreasing neutron fluence seen by them; i.e., S0 and S11 have seen the maximum and minimum neutron fluence, respectively. Another unirradiated sample for reference is assigned as sample number S12. For clarification, refer to Table I. The intensity of the left panels is zoomed for clarity.

defect structures with single and two Frenkel defects in a periodic $4 \times 4 \times 1$ supercell of 64 atoms. The total energy convergence for MD simulations was chosen to 10^{-6} eV; the total energy and forces were calculated using the zone-center point in the Brillouin zone. A time step of 2 fs is used. The simulations were performed for a set of temperatures from 300 to 1100 K using the *NVT* ensemble with Nose thermostat [52]. The simulations are performed up to 100–200 ps. For the defect structures, the starting atomic coordinates as obtained from the relaxed structure with a single or two Frenkel defects is used in a $4 \times 4 \times 1$ supercell. Here we have fixed the unit cell dimensions as obtained from the relaxation of the perfect graphite structure.

IV. RESULTS AND DISCUSSION

A. X-ray and neutron diffraction measurements

The microscopic changes in the structure can be understood from diffraction studies. Figure 1 shows the evolution of the (002), (100), (101), and (004) peaks around the wave-vector transfer $Q \approx 1.84, 2.95, 3.10,$ and 3.70 \AA^{-1} , respectively, in the powder x-ray and neutron diffraction patterns of the irradiated graphite samples. It is evident from this figure that on increasing the neutron fluence, peaks (002) and (004) show appreciable change in position. The peaks are shifted towards lower Q values, which suggests expansion along the c direction ((001)). On the other hand, the (100) peaks show no susceptible change in the peak position and suggest insignificant change along the a direction. To quantify the changes in the lattice parameters, we refined the powder neutron diffraction patterns using hexagonal structure with space group $P6_3/mmc$. Structural parameters obtained from Rietveld refinement are shown in Fig. 2. We find that on

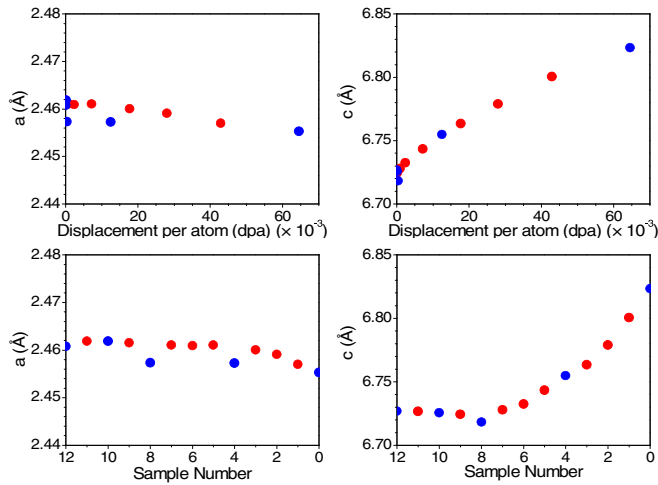


FIG. 2. Variation of the structural parameters of graphite as obtained after Rietveld analyses of x-ray (red closed circles) and combined x-ray and neutron diffraction (blue closed circles) data with displacements per atom (dpa) and sample number. Errors are within symbol size. The irradiated samples are numbered S0–S11 in the order of decreasing neutron fluence seen by them; i.e., S0 and S11 have seen the maximum and minimum neutron fluence, respectively. Another unirradiated sample for reference is assigned as sample number S12. For clarification, refer to Table I.

increasing the neutron fluence, the c lattice parameter shows large expansion and the a lattice parameter shows a small contraction. This is consistent with the nature of bonding in graphite. Graphite is known to have van der Waals bonding along the c axis, which is much weaker than the covalent bonding in the a - b plane.

The analysis of neutron diffraction data (Fig. 2) shows that the graphite samples (S0, ..., S7) that had been irradiated with high neutron fluence (Table I) of epithermal and fast neutrons (exceeding $\sim 10^{19}$ neutrons/cm²) are significantly damaged, while those irradiated with low epithermal and fast neutron fluence but large thermal neutron fluence (S8, ..., S11) are not much damaged. The thermal neutron fluence is not found to be so well correlated with the change in lattice parameters.

B. Differential scanning calorimetry measurements

The plot of heat flux versus temperature for irradiated graphite samples with different doses is shown in Fig. 3. For each sample a single exothermic peak was observed in the temperature range 135 °C–190 °C, which is due to annealing of defects. The values of heat released, temperature range, and exposure doses for various graphite samples are given in Table II. It is clear that the energy released during heating of various samples is related to the absorbed dose. The increase in absorbed dose results in increase in the formation of the defects in the graphite lattice.

C. Topological structures in defected graphite

The experimental neutron diffraction data are shown in Fig. 4(a). It can be seen that peaks in the diffraction patterns of highly irradiated graphite are broader in comparison to that in the fresh sample. These data are analyzed [53] to determine

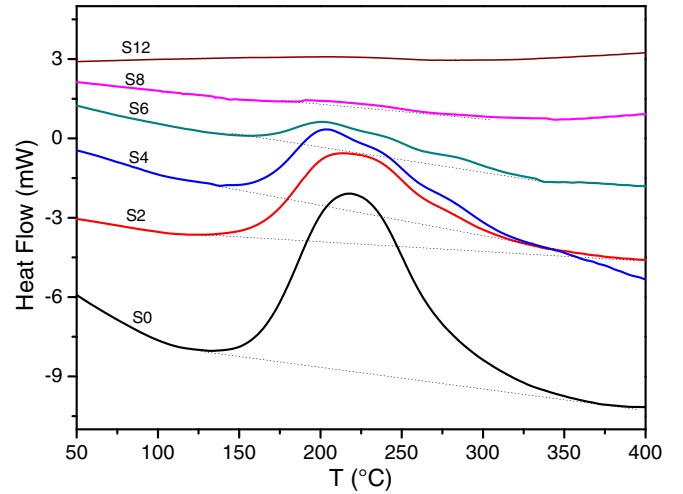


FIG. 3. Heat flow versus temperature for graphite sample irradiated with different fluence of neutron. The irradiated samples are numbered S0–S11 in the order of decreasing neutron fluence seen by them; i.e., S0 and S11 have seen the maximum and minimum neutron fluence, respectively. Another unirradiated sample for reference is assigned as sample number S12. For clarification, refer to Table I.

the real-space pair-distribution function, $g(r)$, which gives the probability of finding neighbors at a distance r . Figure 4(b) shows the pair-distribution function for the unirradiated and several irradiated samples. It is evident from this figure that an additional peak in the $g(r)$ plot of the irradiated samples appears at $r = 2.17$ Å with a redistribution of intensity in the $g(r)$ function. The neutron diffraction results can be understood using *ab initio* simulation of the defect structure. As discussed below we find that this peak arises when an atom in the hexagonal layer is knocked out resulting in a deformed pentagon. The peak at 2.17 Å results from one of the C-C distances in the deformed pentagon from where a vacancy has been created [Fig. 4(c)]. The intensity of the peak at 2.17 Å gradually decreases with decrease of neutron fluence. This provides the experimental evidence for the defect and deformation in the hexagonal structure. In particular, the neutron diffraction data provide evidence of the presence of deformed pentagonal structures and 2-coordinated carbon atoms.

In order to study the defects in graphite we have performed simulation on a $4 \times 4 \times 1$ supercell (comprising two graphite layers and 64 atoms) of the graphite structure. Initially one of the carbon atoms in one of the graphite layers was moved in between the two layers, thus creating a vacancy-interstitial pair, also known as a Frenkel defect. The structural relaxation was performed for this configuration. The relaxed structure is shown in Fig. 4(c). It can be seen that two of the carbon atoms in the hexagon below the interstitial carbon atom form fourfold coordination due to bonding with the interstitial atom (C-C = 1.40–1.52 Å). The atom knocked out from a hexagon results in a deformed pentagon structure, in which one of the second neighbor distances of C-C = 2.45 Å (in the original hexagon) reduces to 2.06 Å (in the deformed pentagon). Three of the carbon atoms now have twofold coordination. The defect structure thus consists [Fig. 4(c)] of 2-, 3-, and 4-coordinated carbon atoms.

TABLE II. The analysis of the data for various samples from differential scanning calorimeter experiments. The irradiated samples are numbered S0–S11 in the order of decreasing neutron fluence seen by them; i.e., S0 and S11 have seen the maximum and minimum neutron fluence, respectively. Another unirradiated sample for reference is assigned as sample number S12. For clarification, refer to Table I. Estimates of the Frenkel defects per atom are shown from the measured Wigner energy from the DSC experiments as well as from the measured c -lattice parameter from our diffraction experiments, based on our *ab initio* calculations of the Wigner energy and c -lattice parameter of defect structures.

Sample No.	Onset temperature for Wigner energy (°C)	Peak temperature for Wigner energy (°C)	End temperature for Wigner energy (°C)	Enthalpy change on release of Wigner energy (J/g)	Frenkel defects per atom from Wigner energy	c (Å)	Δc (Å) with respect to S12	Frenkel defects per atom from Δc
S0	135	218	380	117.9	0.001	6.8234	0.0966	0.0036
S2	135	219	390	82.3	0.0007	6.7789	0.0521	0.0019
S4	139	207	375	75.5	0.00064	6.7547	0.0279	0.001
S6	150	205	350	17.0	0.00014	6.7324	0.0056	0.00021
S12	–	–	–	0	–	6.7268	0	–

We have also simulated a $4 \times 4 \times 2$ (128 atoms) supercell of the graphite structure with one Frenkel defect, which reveals similar defect structure. We note that the small $4 \times 4 \times 1$ supercell is able to capture the essential topological structures of the defects.

We have plotted the pair correlation function [Fig. 4(d)] in the perfect and defect structures used in our calculations. We find that the configurations with one Frenkel defect in 64 atoms or 128 atoms give an additional peak at about 1.5 Å,

which corresponds to the fourfold coordinated carbon atoms. Further, in the $g(r)$ plot we find additional peaks at about 2.06 and 2.15 Å in the defect structure with 64 and 128 atoms, respectively. As discussed above, these peaks correspond [Fig. 4(c)] to one of the second neighbor C-C distances in a deformed pentagon as formed due to a vacancy of carbon atoms.

Reference [32] reported calculations of defect complexes involving defects such as close-proximity vacancies in adjacent layers or interplanar divacancies. However, the present neutron diffraction data could be interpreted in terms of simple well separated Frenkel pairs. Our experimental data do not provide specific signatures of complex interplanar vacancy defects.

We note that larger defects such as dislocations and clusters do not contribute significantly to the neutron diffraction pattern, which essentially results from the crystal structure and the damage at the atomic level. The larger-scale defects do contribute in broadening of the diffraction peaks. Moreover, it seems the Wigner energy is predominantly stored in the interstitial atoms.

D. Phonon spectrum of defected graphite

The measured Raman spectra over 200–1800 cm^{-1} from the fresh and irradiated samples are shown in Fig. 5. These are in agreement with available measurements [29] above 1000 cm^{-1} . We further observe that in the highly irradiated sample there is a large Raman intensity over 400–1000 cm^{-1} with a peak around 800 cm^{-1} . It can be seen that the fresh sample (S12) shows an intense Raman mode at $\sim 1583 \text{ cm}^{-1}$ (G mode), and weak features at around 800 cm^{-1} , $\sim 1355 \text{ cm}^{-1}$ (D mode), and $\sim 1620 \text{ cm}^{-1}$ (D_0 mode). For the maximum irradiated sample, the intensities of these weak features gain very significantly. The intensities of the broad low-energy feature around 800 cm^{-1} and the D mode, and also the peak widths increase significantly for the samples irradiated with very high fluence of the epithermal and fast neutrons.

We note that the perfect graphite structure does not have the D mode. However, the presence of disorder in graphite results in the D mode. Disorder also results in a partial breakdown of the Raman selection rules, which gives some contribution

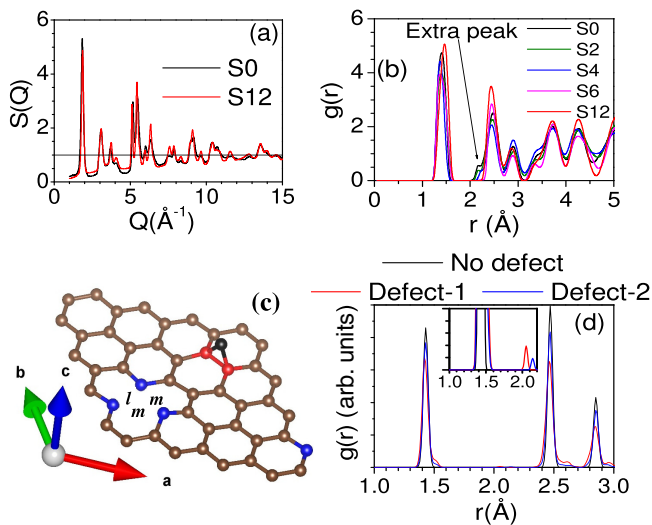


FIG. 4. Topological structures in defected graphite. (a) The neutron diffraction data [$S(Q)$ versus the neutron wave-vector transfer Q] for the unirradiated (S12) and maximum irradiated (S0) samples. (b) The pair-distribution function of irradiated (S0, S2, S4, S6) and unirradiated (S12) graphite as obtained from powder neutron diffraction data. (c) A graphite layer with a single Frenkel defect in a $4 \times 4 \times 1$ supercell. “ l ” and “ m ” correspond to the interatomic distance of 2.06–2.66 Å, respectively. The interstitial atom, and the 2-, 3-, and 4-coordinated carbon atoms are shown by black, blue, brown, and red, respectively. (d) The calculated pair correlation functions in the perfect and defected graphite structures. The labels Defect-1 and Defect-2 indicate the defect structures containing a single Frenkel defect in $4 \times 4 \times 1$ and $4 \times 4 \times 2$ supercells, respectively. In the inset, a part of the figure is zoomed.

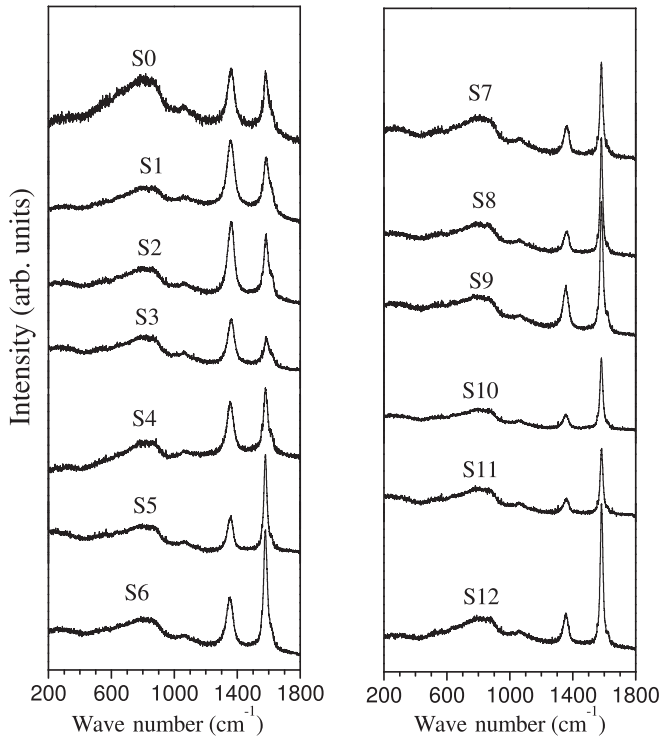


FIG. 5. Measured Raman spectra from graphite samples irradiated at different levels of neutron fluences. The irradiated samples are numbered S0–S11 in the order of decreasing neutron fluence seen by them; i.e., S0 and S11 have seen the maximum and minimum neutron fluence, respectively. Another unirradiated sample for reference is assigned as sample number S12. For clarification, refer to Table I.

from the total phonon density of states in the Raman spectrum. Therefore, we observe Raman intensity at low frequencies, and also the D_0 mode.

The fresh sample (S12) has the D mode with intensity of about 50% of that of the G mode. We further observe that as irradiation level increases there is an increase in Raman intensity of the peak around 800 cm^{-1} and the D mode, and also the peak widths increase significantly for the samples irradiated with very high fluence of the epithermal and fast neutrons. For the maximum irradiated sample (S0), the intensities of the D and G modes are found (Fig. 6) to become almost equal. It can be seen that for a fresh sample the full width at half maximum (FWHM) of the D mode is about 2 times that of the G mode. The FWHM of the peaks of the D and G modes changes with increasing neutron fluence (Fig. 6) and increases significantly for the samples irradiated with very high fluence of the epithermal and fast neutrons.

In order to understand the difference in the phonon spectrum at microscopic level we have calculated the phonon density of states as well as the in-plane and out-of-plane partial components of the phonon density of states in both the perfect and the defect structures. As discussed above, the defect structure with the $4 \times 4 \times 1$ supercell of graphite has 2-, 3-, and 4- coordinated carbon atoms within a graphite layer as well as an interstitial atom in between two layers. We have calculated the partial density of states for each of these types of carbon atoms (Fig. 7).

In the perfect graphite structure, the strong covalent bonding in the a - b plane results in a peak centered at 1364 cm^{-1} , and the out-of-plane vibrations give rise to peaks at 470 and 630 cm^{-1} in the partial component along the c axis. The Raman G mode at $\sim 1583\text{ cm}^{-1}$ does not have much weight in the density of states which represents the integral over the entire Brillouin zone. For the interstitial atom in the defect structure, the in-plane vibrations have a peak at about 320 cm^{-1} , while there is a strong peak of the out-of-plane vibrations at about 850 cm^{-1} with a weaker peak at about 1300 cm^{-1} . The vibrational spectrum of the interstitial atom

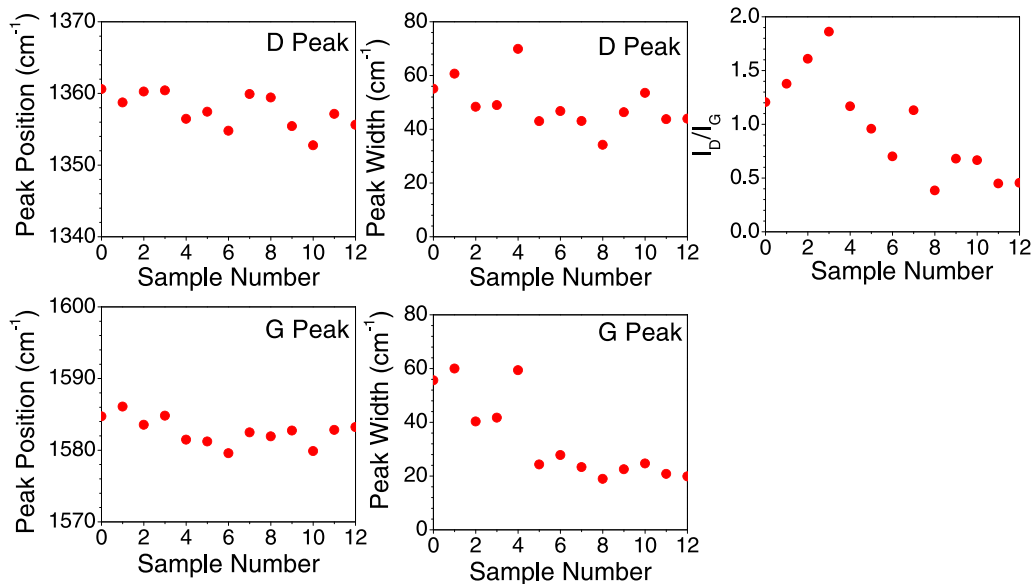


FIG. 6. The peak position and peak width of the D and G peaks in the Raman spectra of the graphite samples, and the intensity ratio (I_D/I_G) of the D and G peaks. The irradiated samples are numbered S0–S11 in the order of decreasing neutron fluence seen by them; i.e., S0 and S11 have seen the maximum and minimum neutron fluence, respectively. Another unirradiated sample for reference is assigned as sample number S12. For clarification, refer to Table I.

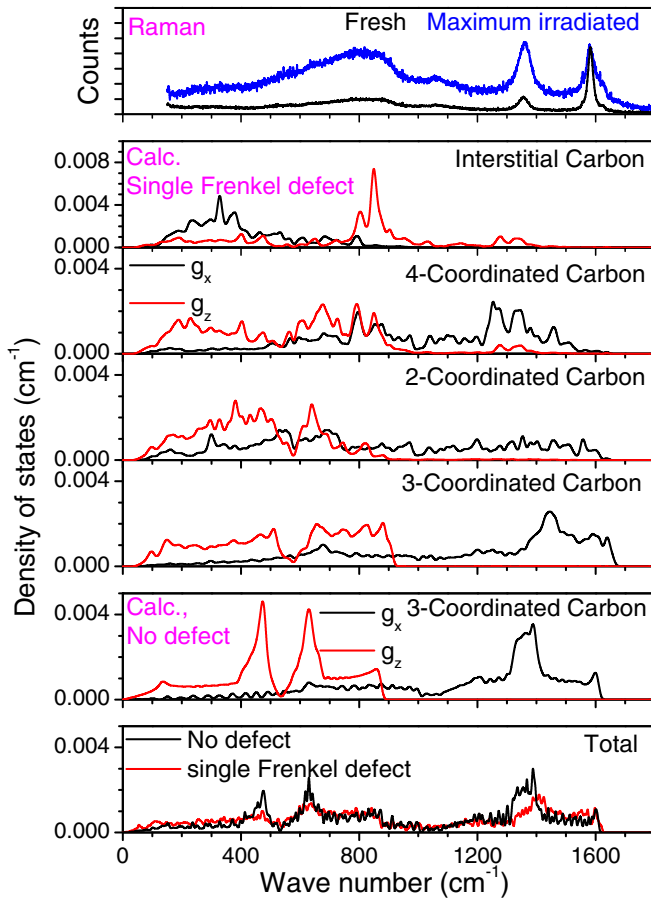


FIG. 7. The measured Raman spectra of the fresh and maximum irradiated graphite sample, and the calculated partial and total phonon density of states of graphite with a single Frenkel defect in a $4 \times 4 \times 1$ supercell and with no defect. g_x and g_z are the x and z components of the partial phonon density of states, respectively.

is quite different from that of the other carbon atoms within a graphite layer in both the in-plane and out-of-plane directions. This may be due to the fact that the interstitial carbon is well bonded along the c axis with another carbon atom, while the in-layer atoms are well bonded within the a - b plane and weakly bonded along the c axis. The out-of-plane vibrational spectra of the in-layer atoms have broad peaks at around 150 – 500 and 650 – 880 cm^{-1} , mainly due to disorder resulting from the removal of an atom in the a - b plane. The in-plane vibrational spectra also show broadening of peaks due to the presence of disorder. Moreover, we find remarkable changes below 500 cm^{-1} , where the intensity of low-energy phonons is more in the spectra of the defect structure.

The changes in the observed Raman spectra (Fig. 7) with irradiation can be understood in terms of the calculated partial phonon density of states of the 2-, 3-, and 4- coordinated carbon atoms in the defect structure. We identify (Fig. 7) that the most prominent increase in the intensity of the D peak at 1360 cm^{-1} is due to the increase in the 4-coordinated carbon atoms. So also, the general increase of the intensity around 800 cm^{-1} may be ascribed to 2- and 3-coordinated carbon defects and the interstitial atom. The results are corroborated

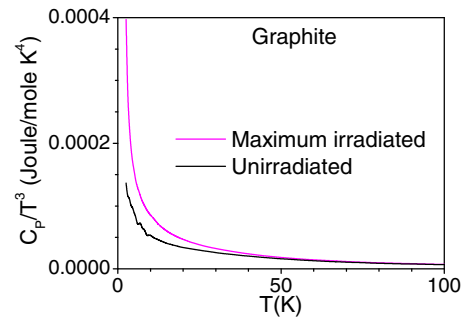


FIG. 8. Specific heat of fresh and irradiated graphite. Comparison of the measured specific heat of unirradiated (sample S12) and maximum irradiated graphite (sample S0).

by simulations on a single Frenkel defect in a $4 \times 4 \times 2$ supercell (Supplemental Material (Fig. S2) [38]).

From *ab initio* calculations of the phonon spectrum in the graphite structure with no defects and that with one Frenkel defect as shown in Fig. 7, we notice that there is considerable softening of low-energy phonons. Such a phonon softening would lead to increase in the specific heat at low temperatures. We indeed found evidence for the same in our measured specific heat (Fig. 8), which clearly shows that the specific heat for the irradiated sample is more in comparison to that of the fresh graphite sample.

E. Annihilation of defects and release of Wigner energy

The recombination of interstitial atoms and vacancies is the key to the release of Wigner energy in graphite. Earlier calculations [32] showed the stored Wigner energy in a Frenkel defect to be about 13 – 15 eV. Reference [26] calculated the energy of a widely separated Frenkel pair to be 13.7 eV, in good agreement with experimental values [54] of about 14 ± 1 eV. They also described an intimate Frenkel pair with a lower energy of 10.8 eV. The release of Wigner energy [12] in experiments is known to complete at about 650 K. We have verified this in our irradiated samples using differential scanning calorimetry (Fig. 3). However, in our simulations, which are performed at a small timescale of ~ 200 ps, the temperature for the defect annihilation is expected to be overestimated. However, simulations are useful to understand the mechanism of annealing of defects in graphite.

We have performed the *ab initio* molecular dynamics simulations of a few different supercell structures with somewhat different interstitial structures. We have kept the interstitial and vacancy as far apart as possible. The topologies of the structures are found to be very similar in all our simulations. However, the choice of the supercell size is limited in the *ab initio* molecular dynamics simulations which are computationally very heavy. An *Ab initio* molecular dynamics simulation of the radiation damage in graphite has been reported [33] that showed a variety of defect formations depending on the selective irradiation conditions, such as controlled direction and magnitude of momentum transfer which is possible in high-energy electron irradiation. Our measurements using neutron irradiation on polycrystalline graphite does not enable control of such irradiation conditions.

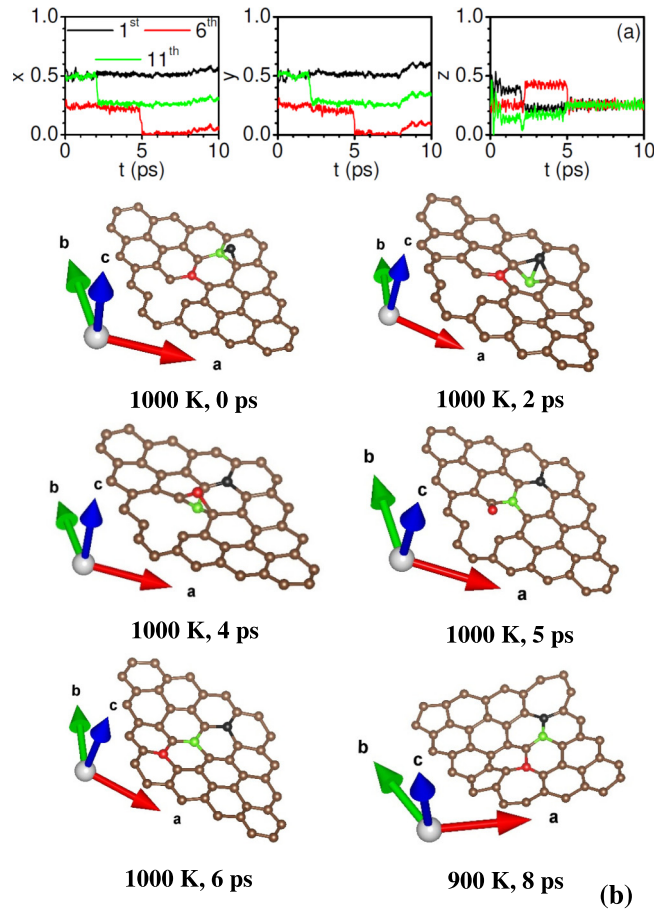


FIG. 9. Annihilation of defects in graphite. Results from *ab initio* molecular dynamics simulations in a $4 \times 4 \times 1$ supercell with a single Frenkel defect at 1000 K. (a) The time dependence of fractional coordinates of the selected three carbon atoms. x , y , and z are the fractional coordinates along the a , b , and c axes, respectively. (b) The snapshots of atoms in one layer of graphite. A snapshot of partially annealed defect at 900 K is also shown. The selected three carbon atoms that are identified as first, sixth, and 11th in panel (a) are shown in (b) by black, red and green circles, respectively.

The simulations are performed on the $4 \times 4 \times 1$ supercell with one Frenkel defect at several temperatures from 300 to 1100 K. The atomic trajectories of carbon atoms have been monitored as a function of time up to 200 ps. Up to 800 K, the defect annihilation process did not start in 200 ps time. However, at 900 K within 7 ps the interstitial carbon atom moved into the graphite layer. At this time, the defect structure at 900 K (Fig. 9) consists of five- and seven-member carbon rings within the graphite layer. The structure did not relax further into hexagonal rings in the simulation up to 200 ps.

In the simulation at 1000 K, the defect energy is completely released in two steps as shown by the time dependence of the atomic coordinates. Figure 9 shows a snapshot of atoms at selected times. First at ~ 2.5 ps through a cooperative movement of neighboring carbon atoms we find that the interstitial carbon atom has moved closer to the vacancy. In the second step at ~ 5.5 ps, the hexagonal structure is restored. The simulations performed at 1100 K showed that within a short time of 1 ps the perfect hexagonal structure is formed.

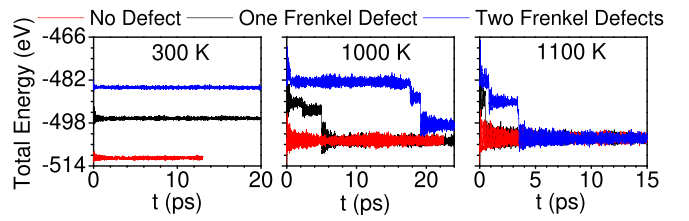


FIG. 10. Annihilation of defects and release of the Wigner energy. The total energy of the $4 \times 4 \times 1$ supercell (64 atoms) as a function of time with a single and two Frenkel defects from *ab initio* molecular dynamics simulations.

The cascading steps of cooperative movement of atoms represent the pathways of the defect annihilation process. (See animations in the Supplemental Material [38], which provide visualization of the likely different mechanisms of annealing of defects in multiple steps as discussed above.)

We have calculated the total energy of the supercell as a function of time, which reveals the Wigner energy released during the defect annihilation process (Fig. 10). We find the Wigner energy at any temperature to be ~ 15 eV per vacancy-interstitial defect pair, which is in good agreement with earlier calculations of 13–15 eV [26,32] and an experimental value [54] of about 14 ± 1 eV. However, a significant energy barrier prevents the annealing of the defect at a timescale of 200 ps up to 800 K. However, at 900 K we found that, although the interstitial carbon atom moves in the graphite layer, the structure does not fully anneal in 200 ps time, and still retains a potential energy of about 5 eV. At 1000 K, the energy of 15 eV is released during the defect annihilation in two steps (Fig. 10), while at 1100 K the same energy is released in a single step.

We have also performed the MD simulations with a structure consisting of two Frenkel defects (Fig. 10) in the $4 \times 4 \times 1$ supercell. Here we created one Frenkel defect each in both the graphite layers in the supercell such that the vacancies and defects are sufficiently apart (see animations in the Supplemental Material [38]). In two Frenkel defects the stored Wigner energy is calculated to be ~ 26.4 eV. We found that at 1000 K one Frenkel defect has annealed at ~ 17.5 ps, while the second Frenkel defect is not fully annealed until 100 ps as it forms a pair of five- and seven-member rings. However, at 1100 K we found annealing of both the Frenkel defects in 4 ps. The annihilation of the first Frenkel defect releases about 10–11 eV of energy while that of the second Frenkel defect releases about 15 eV (see animations in the Supplemental Material [38]).

Assuming that the defects are mostly simple Frenkel defects, we have estimated the concentration of Frenkel defects per atom in our samples. This is done in two different ways, which also helps to perform a self-consistency check. One estimate is obtained from the calorimetry measurements of the Wigner energy and the *ab initio* calculated defect energy of 15 eV of a single Frenkel defect. Another estimate is obtained from the measured lattice parameters from the diffraction experiments and the *ab initio* calculations of the lattice parameters of various defect structures. Table S1 in the Supplemental Material [38] gives the calculated lattice parameters of the structures with a single Frenkel defect in $4 \times 4 \times 1$ and $4 \times 4 \times 2$ supercells, as well with two Frenkel

defects in $4 \times 4 \times 1$ supercell. Compared to the perfect graphite structure, we find that for the defect structure the a -lattice parameter changes only slightly, while the c -lattice parameter increases substantially. We have, therefore, estimated the defect concentration by comparing the measured and calculated changes in the c -lattice parameters. The results are given in Table II, which show that the two estimates of the Frenkel defects per atom are of the same order of magnitude, which is very satisfactory given the limitations of the calculations on rather small supercells.

However, the difference between the two estimates is more for samples S0 and S2 with larger neutron dose. If we assume that the estimate from the measured lattice parameters is correct, it would imply that the Wigner energy per defect for these samples is lower than 15 eV. These samples have a higher concentration of Frenkel defects. It is possible to have a lower average Wigner energy per defect if we have clusters of Frenkel defects rather than only the isolated ones. This is apparent from the *ab initio* calculation, which indicates that the Wigner energy per defect for a single and double Frenkel defect is about 15 and 13 eV, respectively.

V. CONCLUSIONS

In this paper, we have provided direct characterization of defects in neutron-irradiated graphite through neutron diffraction, Raman scattering, and specific heat measurements, and complemented the results by *ab initio* simulations. The measurements show that the graphite samples which have been irradiated with very high neutron fluence of epithermal and fast neutrons are damaged significantly, while the thermal neutron fluence is not so well correlated. Specifically, we

have observed signatures of 2-, 3-, and 4-coordinated carbon topologies around the Frenkel defects in both the diffraction and Raman experiments. The microscopic understanding of annealing of defects on heating is achieved through *ab initio* molecular dynamics simulations. These involve cooperative movement of atoms in several cascading steps depending on the distance between the vacancy and interstitial positions. The experimental and theoretical work has provided valuable insights in understanding of the structure and dynamical behavior of the defects in neutron-irradiated graphite, the annihilation of the defects, and consequently release of unusually large Wigner energy.

We note from our *ab initio* simulations on various supercells that the defect structure in a graphite layer around a Frenkel defect is essentially independent of the separation of such defects along the hexagonal c axis. This may be expected due to the much weaker van der Waals interaction between the graphite layers compared to the strong covalent bonding within the layers. Other graphitic materials including graphene and carbon nanotubes have similar two-dimensional structure and bonding as in a graphite layer, and these may also be used in a high-radiation environment including outer space. Therefore, the present work on highly irradiated graphite is of considerable importance to wider areas of graphitic materials.

ACKNOWLEDGMENTS

The use of ANUPAM supercomputing facility at BARC is acknowledged. S.L.C. acknowledges the financial support of the Indian National Science Academy for a INSA Senior Scientist position.

-
- [1] International Atomic Energy Agency, Report No. IAEA-TECDOC-1521 (IAEA, Vienna, 2006).
 - [2] J. H. W. Simmons, *Radiation Damage in Graphite: International Series of Monographs in Nuclear Energy* (Elsevier, Amsterdam, 2013), Vol. 102.
 - [3] P. O. Lehtinen, A. S. Foster, Y. Ma, A. V. Krasheninnikov, and R. M. Nieminen, *Phys. Rev. Lett.* **93**, 187202 (2004).
 - [4] F. Banhart, *Rep. Prog. Phys.* **62**, 1181 (1999).
 - [5] B. Peng, M. Locascio, P. Zapol, S. Li, S. L. Mielke, G. C. Schatz, and H. D. Espinosa, *Nat. Nanotechnol.* **3**, 626 (2008).
 - [6] A. V. Krasheninnikov, K. Nordlund, and J. Keinonen, *Phys. Rev. B* **65**, 165423 (2002).
 - [7] O. Lehtinen, J. Kotakoski, A. V. Krasheninnikov, A. Tolvanen, K. Nordlund, and J. Keinonen, *Phys. Rev. B* **81**, 153401 (2010).
 - [8] J.-H. Chen, W. G. Cullen, C. Jang, M. S. Fuhrer, and E. D. Williams, *Phys. Rev. Lett.* **102**, 236805 (2009).
 - [9] A. Krasheninnikov and F. Banhart, *Nat. Mater.* **6**, 723 (2007).
 - [10] J. Lin, Z. Peng, Y. Liu, F. Ruiz-Zepeda, R. Ye, E. L. Samuel, M. J. Yacaman, B. I. Yakobson, and J. M. Tour, *Nat. Commun.* **5**, 5714 (2014).
 - [11] H. S. Lipson and A. Stokes, *Proc. R. Soc. London, Ser. A* **181**, 101 (1942).
 - [12] T. Iwata, *J. Nucl. Mater.* **133-134**, 361 (1985).
 - [13] P. de Andres, F. Guinea, and M. I. Katsnelson, *Phys. Rev. B* **86**, 245409 (2012).
 - [14] O. Blakslee, D. Proctor, E. Seldin, G. Spence, and T. Weng, *J. Appl. Phys.* **41**, 3373 (1970).
 - [15] B. Marsden, A. Mummery, and P. Mummery, *Proc. R. Soc. London, Ser. A* **474**, 20180075 (2018).
 - [16] F. Entwisle, *Phys. Lett.* **2**, 236 (1962).
 - [17] Y. Baskin and L. Meyer, *Phys. Rev.* **100**, 544 (1955).
 - [18] J. Nelson and D. Riley, *Proc. Phys. Soc.* **57**, 477 (1945).
 - [19] P. Giura, N. Bonini, G. Creff, J. B. Brubach, P. Roy, and M. Lazzeri, *Phys. Rev. B* **86**, 121404(R) (2012).
 - [20] S. Rols, Z. Benes, E. Anglaret, J. L. Sauvajol, P. Papanek, J. E. Fischer, G. Coddens, H. Schober, and A. J. Dianoux, *Phys. Rev. Lett.* **85**, 5222 (2000).
 - [21] J.-B. Wu, M.-L. Lin, X. Cong, H.-N. Liu, and P.-H. Tan, *Chem. Soc. Rev.* **47**, 1822 (2018).
 - [22] I. I. Al-Qasir, A. A. Campbell, G. Sala, J. Y. Lin, Y. Cheng, F. F. Islam, D. L. Abernathy, and M. B. Stone, *Carbon* **168**, 42 (2020).
 - [23] L. Arnold, *Windscale 1957: Anatomy of a Nuclear Accident* (Springer, Berlin, 2016).
 - [24] B. Kelly, *Physics of Graphite* (Applied Science, London/New Jersey, 1981), p. 267.
 - [25] E. Kaxiras and K. C. Pandey, *Phys. Rev. Lett.* **61**, 2693 (1988).
 - [26] C. P. Ewels, R. H. Telling, A. A. El-Barbary, M. I. Heggie, and P. R. Briddon, *Phys. Rev. Lett.* **91**, 025505 (2003).
 - [27] B. Marsden, M. Haverly, W. Bodel, G. Hall, A. Jones, P. Mummery, and M. Treifi, *Int. Mater. Rev.* **61**, 155 (2016).

- [28] D. McEligot, W. D. Swank, D. L. Cottle, and F. I. Valentin, Thermal Properties of G-348 Graphite, U.S. Department of Energy Report No. INL/EXT-16-38241 (2016).
- [29] R. Krishna, A. Jones, L. McDermott, and B. Marsden, *J. Nucl. Mater.* **467**, 557 (2015).
- [30] R. Telling and M. Heggie, *Philos. Mag.* **87**, 4797 (2007).
- [31] A. McKenna, *Ab initio* and molecular dynamic models of displacement damage in crystalline and turbostratic graphite, Ph.D. thesis, University of Surrey, 2016.
- [32] R. H. Telling, C. P. Ewels, A. Ahlam, and M. I. Heggie, *Nat. Mater.* **2**, 333 (2003).
- [33] O. V. Yazyev, I. Tavernelli, U. Rothlisberger, and L. Helm, *Phys. Rev. B* **75**, 115418 (2007).
- [34] I. Mosyagin, D. Gambino, D. G. Sangiovanni, I. A. Abrikosov, and N. M. Caffrey, *Phys. Rev. B* **98**, 174103 (2018).
- [35] L. Li, S. Reich, and J. Robertson, *Phys. Rev. B* **72**, 184109 (2005).
- [36] R. Ranjan, S. Bhattacharya, P. V. Varde, C. G. Karhadkar, P. Mandal, M. K. Ojha, G. K. Mallik, and V. D. Alur, BARC Report (External) No. BARC/2017/E/006 (Bhabha Atomic Research Centre, Mumbai, 2017).
- [37] T. D. Burchell, *Carbon Materials for Advanced Technologies* (Elsevier, Amsterdam, 1999).
- [38] See Supplemental Material at <http://link.aps.org/supplemental/10.1103/PhysRevB.102.064103> for details about small angle x-ray scattering measurements. Supplemental Material includes the results of calculation of the phonon spectra for a single Frenkel defect in a $4 \times 4 \times 2$ supercell, and the results of the total energy of a $4 \times 4 \times 1$ supercell (64 atoms) with a single and two Frenkel defects as a function of time from *ab initio* molecular dynamics simulations. Animations showing the annihilation of defects in graphite at different temperature in various simulation cells are given in separate files in the Supplemental Material. (See, also, Refs. [1–5] therein).
- [39] H. Rietveld, *J. Appl. Crystallogr.* **2**, 65 (1969).
- [40] J. Rodríguez-Carvajal, *Physica B* **192**, 55 (1993).
- [41] B. Dasannacharya, *Phys. B (Amsterdam, Neth.)* **180-181**, 880 (1992).
- [42] L. Pusztai and R. McGreevy, *Phys. B (Amsterdam, Neth.)* **234-236**, 357 (1997).
- [43] G. Kresse and J. Furthmüller, *Comput. Mater. Sci.* **6**, 15 (1996).
- [44] G. Kresse and D. Joubert, *Phys. Rev. B* **59**, 1758 (1999).
- [45] J. P. Perdew, K. Burke, and M. Ernzerhof, *Phys. Rev. Lett.* **78**, 1396 (1997).
- [46] J. P. Perdew, K. Burke, and M. Ernzerhof, *Phys. Rev. Lett.* **77**, 3865 (1996).
- [47] H. J. Monkhorst and J. D. Pack, *Phys. Rev. B* **13**, 5188 (1976).
- [48] M. Dion, H. Rydberg, E. Schröder, D. C. Langreth, and B. I. Lundqvist, *Phys. Rev. Lett.* **92**, 246401 (2004).
- [49] K. Lee, É. D. Murray, L. Kong, B. I. Lundqvist, and D. C. Langreth, *Phys. Rev. B* **82**, 081101(R) (2010).
- [50] J. Klimeš, D. R. Bowler, and A. Michaelides, *Phys. Rev. B* **83**, 195131 (2011).
- [51] K. Parlinski, PHONON software, 2003.
- [52] S. Nosé, *J. Chem. Phys.* **81**, 511 (1984).
- [53] L. Van Hove, *Phys. Rev.* **95**, 249 (1954).
- [54] P. Thrower and R. Mayer, *Phys. Status Solidi A* **47**, 11 (1978).